

PAPER

Modeling non-equilibrium discharge and validating transient plasma characteristics at above-atmospheric pressure

To cite this article: Riccardo Scarcelli *et al* 2018 *Plasma Sources Sci. Technol.* **27** 124006

View the [article online](#) for updates and enhancements.



IOP | ebooks™

Bringing you innovative digital publishing with leading voices to create your essential collection of books in STEM research.

Start exploring the collection - download the first chapter of every title for free.

Modeling non-equilibrium discharge and validating transient plasma characteristics at above-atmospheric pressure

Riccardo Scarcelli¹ , Thomas Wallner¹, Sibendu Som¹, Sayan Biswas² , Isaac Ekoto², Douglas Breden³, Anand Karpatne³ and Laxminarayan L Raja⁴

¹ Argonne National Laboratory, United States of America

² Sandia National Laboratories, United States of America

³ Esgee Technologies, United States of America

⁴ The University of Texas at Austin, United States of America

Received 26 June 2018, revised 10 September 2018

Accepted for publication 29 November 2018

Published 28 December 2018



CrossMark

Abstract

Non-equilibrium plasma generated from positive-pulsed nanosecond electrical discharges into desiccated air is simulated in this paper using a multi-dimensional, multi-physics plasma solver. A pin-to-pin electrode configuration is used with a fixed 5.2 mm gap spacing. Peak pulse voltages range between 10.2 and 22.5 kV. Care is taken to match the exact electrode profile from the experiments, and adjust the electron collision frequency so that breakdown limits closely match those from corresponding experimental results. The optimized numerical simulations predict qualitative streamer structure that is in close agreement with experimental observations. Quantitative measurements of atomic oxygen at the anode tip and qualitative estimates of streamer gas heating are closely matched by simulations. The model results are used to provide insight into the spatial and temporal development of the transient plasma. The work performed in this paper delivers a numerical tool that can be extremely useful to link the post-discharge plasma properties to low-temperature plasma ignition mechanisms that are of great interest for the automotive industry.

Keywords: non-equilibrium plasma, multi-dimensional modeling, plasma assisted ignition

Introduction

Following the technological development of spark-ignition internal combustion engines (ICEs), non-conventional ignition technologies are being increasingly considered as a potential replacement for conventional inductive or capacitive spark-based ignition systems [1]. Among those technologies, low-temperature plasma (LTP), also known as non-equilibrium plasma, attracts the highest interest from automotive OEMs due to promising performance [2, 3] and lack of significant technological barriers affecting the operation of other ignition systems (e.g. the lens fouling issue generated by laser systems). In particular, LTP does not induce significant heating at the electrode surface, which helps to increase the ignition hardware lifetime and reduce the ignition energy lost through heat transfer.

Research on plasma assisted ignition and combustion (PAI) has been intensively carried out for more than a decade [4, 5]. Nevertheless, the application of LTP to engine ignition processes is still very novel. Most of the existing literature on LTP modeling focuses on low-pressure applications [5], where the plasma characteristics are fairly uniform in space, and 0-D chemistry solvers can trace the evolution of the most relevant chemical species (including electrons, ions, radicals, atoms, and molecules, in their ground or excited state) with relatively short computational run times. However, engine applications are characterized by above-atmospheric pressures and temperatures, especially in a PAI mode. As a result, generated plasma streamers are non-uniform, with a broad distribution of chemical and thermal properties. Within the engine research community, a number of PAI systems have been investigated including microwaves [6, 7], radio-frequency (RF) discharges

Table 1. Calorimeter specifications and operating conditions.

Internal volume (cm ³)	29
Distance between electrodes (mm)	5.2
Initial temperature (°C)	70
Initial pressure (bar)	1.2–3.4
Voltage (kV)	10.3–22.5
Mixture composition (% volume)	20.95% O ₂ , 79.05% N ₂

[8, 9], and nanosecond pulsed discharges [10, 11]. The nanosecond pulsed discharge, or transient plasma, is of particular interest because of its potential for higher reduced electric field (E/N) values with respect to microwaves or RF discharges. Higher E/N leads to higher ionization and dissociation rates with lower energy utilization rates.

Pai *et al* [12] parametrically studied repetitively pulsed nanosecond discharges in air at atmospheric pressure, and have confirmed the existence of three distinctive regimes, namely the corona, glow, and spark regimes. The spark regime introduces substantial gas heating and generates a high-current, luminous electrical arc. Electrical energy for the arcing discharges in the spark regime is more efficiently converted into thermal energy that results in electrode surface erosion. Both corona and glow regimes are non-thermal discharges. The glow regime occupies a larger spatial region across the discharge gap, while the corona regime is limited to the vicinity of the anode. The more diffuse glow regime is thus attractive for advanced ignition systems. Recently, Wolk and Ekoto have presented experimental observations of single- and multi-pulse nanosecond discharges in air at room temperature and pressure values from 1 to 9 bar [13, 14]. They focused their research on identifying the mechanism for transition from glow to spark regime in a multi-pulse discharge. Also, they characterized the transition from glow to spark regime for a single-pulse discharge. Finally, they provided qualitative analysis of the distribution of atomic oxygen (excited state) and temperature in the glow phase, using direct imaging and schlieren technique respectively.

As of today, computational fluid dynamics (CFD) tools used for ICE multi-dimensional simulations do not offer LTP ignition models. The LTP ignition mechanism is quite different from the conventional, thermal ignition mechanism. In the former, ignition is triggered by the increase of the concentration of active species such as radicals, ions, and excited molecules rather than local high temperature values [15]. As an example, atomic oxygen (O) has been experimentally identified as a product of nanosecond pulsed discharge, which also features long enough lifetime to influence hydrocarbon combustion reactions [11]. Overall, state-of-the-art ignition models implemented in engine CFD solvers cannot be used to describe LTP ignition mechanism, and new conceptual models need to be developed. To this aim, the key question concerns the characteristics of the plasma at the end of the electrical discharge. It is known that in a transient plasma there can be significant non-equilibrium in the species composition, with a large disparity in the electron temperature that can be much higher than the translational temperature of the

heavier species in the plasma. In addition, other degrees of freedom in the plasma such as vibrationally excited molecules can exist that are themselves characterized by different temperatures from the electron and heavy species translational temperatures. This complicates the description of combustion chemistry that has traditionally relied on a temperature single-value assumption for determining species production/destruction rates. From a combustion modeling perspective, when using the Arrhenius correlation for the reaction rate, the key information that is needed includes temperature and concentration of the reactants. At above-atmospheric conditions, these quantities are not uniform in space.

Multi-dimensional LTP modeling has been recently performed in a detailed fashion, although for very simple geometries. Among the most significant contributions that can be found in literature, Tholin and Bourdon performed a series of numerical studies [16, 17] on the glow regime of repetitively pulsed nanosecond discharge from two pin electrodes in atmospheric air, which are in direct comparison with the experimental studies of Pai *et al* [12]. They have analyzed the streamer characteristics in terms of propagation speed and the conditions for transitions into the spark or corona regimes. Furthermore, they have mimicked the multi-pulse behavior of the non-equilibrium discharge and investigated the conditions for the plasma to remain in a glow phase. Recently, the authors of this paper have conducted initial LTP multi-dimensional simulation studies [18] based on the experiments carried out by Wolk and Ekoto [14]. The electrode geometry and gap spacing were matched to the experiment, with the measured voltage signal used as the simulation input boundary condition. Predicted distributions of local gas heating and chemically reactive species like atomic oxygen were successfully compared to qualitative images of temperature gradients using the schlieren technique and electronically excited states of atomic oxygen using direct imaging. Also, the LTP transition into the spark regime (i.e. arcing condition) was mapped out as a function of initial pressure, with the results compared to the experiments. Overall, the model showed good accuracy, although the transition pressure was not perfectly matched by the simulations.

This paper expands our previous research efforts and has two main objectives: (1) reduce or eliminate the discrepancy between modeling and experiments in terms of LTP-to-arc transition pressure; (2) provide a quantitative validation of the plasma thermal and chemical characteristics. To this aim, better control on the gas composition, geometry of the electrodes, and voltage measurements was achieved. Parametric simulations were performed, with model constants tuned to match the experiments. Finally, the quantitative comparison of relevant quantities such as temperature and atomic oxygen concentration, between simulations and experiments, was carried out at the same location.

Experimental setup and conditions

The experimental apparatus was previously discussed in detail by Wolk and Ekoto [13, 14], therefore only a brief

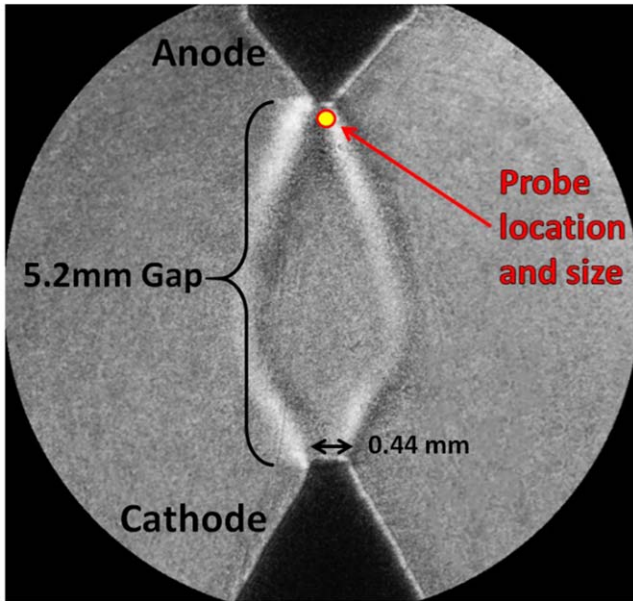


Figure 1 Detail of electrodes position and location of the probe for experimental sampling.

description is presented here. All experiments were performed in a stainless steel 316 custom-built, optically accessible, spark calorimeter with an internal volume of 29 cm³. During the experiment, the initial calorimeter temperature, T_{initial} , was heated to a temperature of 70 °C (343 K) using resistive heating tape with the temperature monitored using embedded K-type thermocouples. The calorimeter was filled up to the desired pressure (up to 3.4 bar absolute, for this case) using desiccated air with 20.95% O₂ by volume. Key specifications and operating conditions of the calorimeter are reported in table 1. To generate the pulse nanosecond discharges within the calorimeter, a Transient Plasma Systems Inc. SSPG-101-HF high-voltage (28 kV peak) pulse generator with a 12 ns full width at half max pulse width and a 5 ns rise time was used. A low-impedance inline attenuator was used to monitor pulse voltage and current for each discharge event.

The relative position of the anode and cathode is schematically shown in figure 1. The high-voltage anode was built by modifying an NGK DP7EA-9 size M12 non-resistive spark plug. The plug J-hook and top 1 cm of the outer body ground were removed, with the anode tip machined to a rounded point ($\sim 125 \mu\text{m}$ radius of curvature) to maximize the local electric field strengths, while maintaining relatively repeatable discharge characteristics. The anode was centrally positioned at the top of the calorimeter. A sharpened 3.18 mm diameter stainless steel rod was used as the cathode. The cathode was installed from the calorimeter base and secured in place by a Swagelok fitting. A constant inter-electrode distance of 5.2 mm was maintained throughout for the present study. It is worth noting that, different from the anode, the cathode has a flat top circular tip and the dimension ($\phi = 0.44 \text{ mm}$) was measured experimentally. Figure 1 also shows the location (0.1 mm below the anode tip) and size (0.5 mm diameter) of the domain used for O-TALIF measurement of the atomic oxygen (ground state)

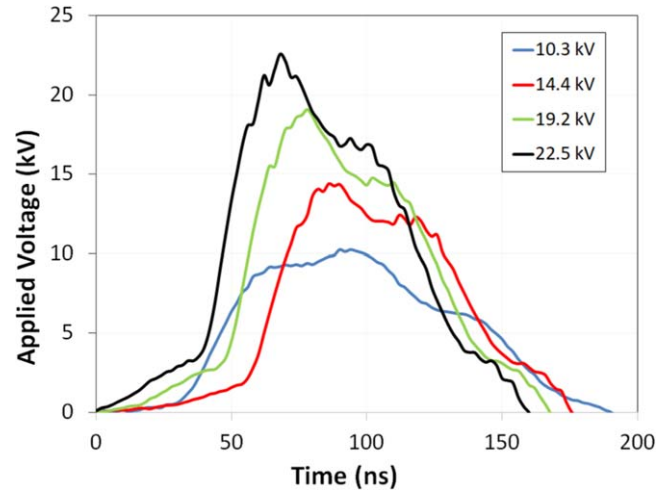


Figure 2. Voltage profile traces measured in experiments and used as boundary conditions for transient plasma simulations.

Table 2. Experimental conditions evaluated for model validation.

#	Voltage (kV)	Above-arc absolute pressure (bar)
1	10.3	1.2
2	14.4	1.5
3	19.2	2.0
4	22.5	3.4

concentration. Simulations results were probed at the same location/size.

The experimental conditions evaluated for model validation are listed in table 2. These conditions explored the LTP characteristics, just above the pressure threshold that identifies the transition from spark (arc) to glow (LTP) regime, when the peak voltage was varied between 10.3 and 22.5 kV. The corresponding initial pressure was varied between 1.2 and 3.4 bar absolute with initial temperature fixed at 70 °C. For these conditions, the chamber gas densities were similar to the densities encountered in a naturally aspirated engine for very early spark timings [2]. The above-arc pressure value shown in table 2 represents the lowest value of initial pressure that is needed to completely avoid spark.

Measured profiles of voltage are plotted in figure 2. The assumption made in simulations, which is also verified by experiments, is that the voltage profile does not change even if the initial pressure changes unless an arc event (plasma in the spark regime) is detected. Also, only the main pulse is simulated, since the subsequent voltage oscillations (also referred as to ringing) have a relatively lower impact. This assumption will be discussed later in the paper.

Numerical model setup

Plasma modeling

The transient plasma simulations performed in this paper are carried out using the commercial non-equilibrium plasma solver VizGlow, version 2.1 [19]. VizGlow is a general

purpose self-consistent, multi-species, multi-temperature plasma solver developed by Esgee Technologies Inc., which can be specialized to describe the high-pressure streamer as well as corona discharge [20]. Poisson's equation is solved for the self-consistent electrostatic field in the plasma. In addition, a number of differential equations are solved that account for the production/destruction and transport of multiple charged and neutral species along with the electron and bulk gas energy distribution. The model also accounts for the photoionization process which is an important source of background electrons for the streamer propagation in air mixtures, in particular for streamers generated from positive electrodes (also referred as to positive streamers).

Species continuity equation is formulated as follows:

$$\frac{\partial n_k}{\partial t} + \vec{\nabla} \cdot \vec{\Gamma}_k = \dot{G}_k, \quad (1)$$

where k is the species index. All involved species are solved for except for the dominant background neutral species. The number density of the dominant background species is calculated from the ideal gas law at a specified total gas pressure and gas temperature, by subtracting all other species. The gas chemistry source term, \dot{G}_k , is calculated using a finite-rate chemistry mechanism.

The species number flux term $\vec{\Gamma}_k$ is obtained using the drift-diffusion approximation formulated below:

$$\vec{\Gamma}_k = n_k \vec{u}_k = \mu_k n_k \vec{E} - D_k \vec{\nabla} n_k. \quad (2)$$

The drift-diffusion approximation is accurate at pressures of 100 mTorr and higher and at room temperature when the mean free path of the species (on order of μm) are much smaller than the characteristics length scales of the geometry (on order of mm).

The electrostatic potential ϕ is calculated by solving Poisson's equation:

$$\nabla^2 \phi = -\frac{e}{\varepsilon_0 \varepsilon_r} \sum_k Z_k n_k, \quad (3)$$

where ε_0 is the permittivity of free space, ε_r is the relative permittivity of the material, and Z_k is the charge number of the individual species k . The relative permittivity is 1 for the gas domain. The charge number is -1 for electrons, $+1$ for all singly ionized positive ions and -1 for singly charged negative ions.

Electron energy transport is accounted for by solving the electron temperature using the electron energy conservation equation:

$$\begin{aligned} \frac{\partial e_e}{\partial t} + \vec{\nabla} \cdot ((e_e + p_e) \vec{u}_e - \kappa_e \vec{\nabla} T_e) &= e \vec{\Gamma}_e \cdot \vec{\nabla} \phi \\ - e \sum_i \cdot E_i^e r_i - \frac{3}{2} k_B n_e \frac{2m_e}{m_b} (T_e - T_g) \bar{v}_e. \end{aligned} \quad (4)$$

The total electron energy is assumed to be approximately equal to the mean electron energy $e_e = \frac{3}{2} k_B n_e T_e$, while the electron pressure p_e is obtained using the ideal gas law. The right-hand side of the electron energy equation incorporates

three source terms: Joule heating, inelastic collisional heating, and elastic collisional heating, respectively.

The bulk temperature is obtained by solving the energy conservation equation:

$$\begin{aligned} \frac{\partial e_h}{\partial t} + \vec{\nabla} \cdot (-\kappa_h \vec{\nabla} T_h) &= \sum_k e Z_k \vec{\Gamma}_k \cdot \vec{\nabla} \phi \\ + \frac{3}{2} k_B n_e \frac{2m_e}{m_b} (T_e - T_h) \bar{v}_e - e \sum_i \cdot E_i^h r_i. \end{aligned} \quad (5)$$

Here bulk energy per unit volume $e_h = C_v T_h$ is assumed to be the same for all heavy species. κ_h is the bulk thermal conductivity. This equation includes the effect of several source terms (shown on the right-hand side). The first source term represents summation of Joule heating over all ion species k . The second term is a measure of the bulk energy gain due to elastic collisions of between heavy species and electrons. Further, heat loss due to inelastic collisions is calculated by performing a summation over all heavy species reactions. Here, ΔE_i^h is the loss of heavy species energy per collision and r_i is the rate of progress for reaction ' i '. The simulations performed in this study leverage the assumption that the bulk fluid motion is omitted, due to the small temporal scale of the discharge. Therefore, local mean velocity, \vec{u}_h , is equal to zero and does not appear in equation (5), while pressure is fixed.

In this work, the boundary conditions imposed on this problem are at solid surfaces, the axis line and the outer ambient. At solid walls, the flux of each species to and from the wall is imposed. For every species k , the one-directional temperature dependent Maxwellian flux normal to the wall which can be written as

$$\vec{\Gamma}_k \cdot \hat{n} = \frac{1}{4} n_k \sqrt{\frac{8k_b T_k}{\pi m_k}}, \quad (6)$$

where T_k is the temperature of species k , k_b is Boltzmann's constant, n_k is the volumetric number density of species k and m_k is the species mass. The unit direction normal into the wall is \hat{n} .

Electrons may be emitted from the wall when other species i impact the wall in a process known as secondary electron emission.

$$\Gamma_{e,\text{secondary}} \cdot \hat{n} = -\sum_i \gamma_i \Gamma_i \cdot \hat{n}, \quad (7)$$

where the incoming flux of species i is $\vec{\Gamma}_i$, the secondary emission coefficient representing number of electrons emitted per impacting particle i is γ_i and the minus sign indicates that electrons are being emitted away from the wall into the plasma.

For charged ion species, if the product of the electric field and the species charge number is directed towards the wall (indicating bombardment) and additional wall flux term $\Gamma_{k,\text{bombardment}}$ is included

$$\Gamma_{k,\text{bombardment}} \cdot \hat{n} = n_k Z_k E \cdot \hat{n} \quad \text{if } Z_k E \cdot \hat{n} > 0. \quad (8)$$

Electron's impact the wall each carry an energy of $2k_b T_e$ Joules of energy. For electrons emitted from the wall due to secondary impact, each electron carries with it an energy of $e \Delta E_{e,k}$ Joules. The term $\Delta E_{e,k}$ is the energy in eV that each

Table 3. Reactions of the plasma detailed mechanism used in this study.

Rxn	Reaction	A (molecules-m)	B (non-dim)	C (Kelvin)	$\Delta E_{\text{electron}}$ (eV)	$\Delta E_{\text{background}}$ (eV)
G ₁	E + N ₂ -> E + N ₂ (rotational)	BOLSIG+			-0.02	0.02
G ₂	E + N ₂ -> E + N ₂ (vibrational)	BOLSIG+			-1.0	1.0
G ₃	E + N ₂ -> E + N ₂ A	BOLSIG+			-6.17	—
G ₄	E + N ₂ -> E + N ₂ B	BOLSIG+			-7.35	—
G ₅	E + N ₂ -> E + N ₂ B	BOLSIG+			-7.36	—
G ₆	E + N ₂ -> E + N ₂ B	BOLSIG+			-8.16	—
G ₇	E + N ₂ -> E + N ₂ a1	BOLSIG+			-8.4	—
G ₈	E + N ₂ -> E + N ₂ a1	BOLSIG+			-8.55	—
G ₉	E + N ₂ -> E + N ₂ a1	BOLSIG+			-8.89	—
G ₁₀	E + N ₂ -> E + N ₂ C	BOLSIG+			-11.03	—
G ₁₁	E + N ₂ -> E + N ₂ (electronic exc.)	BOLSIG+			-11.88	11.88
G ₁₂	E + N ₂ -> E + N ₂ (electronic exc.)	BOLSIG+			-12.25	12.25
G ₁₃	E + N ₂ -> E + N ₂ (electronic exc.)	BOLSIG+			-13.0	13.0
G ₁₄	E + N ₂ -> 2E + N ₂ ⁺	BOLSIG+			-15.6	—
G ₁₅	E + O ₂ -> E + O ₂ (rotational)	BOLSIG+			-0.02	0.02
G ₁₆	E + O ₂ -> E + O ₂ (vibrational)	BOLSIG+			-0.193	0.193
G ₁₇	E + O ₂ -> E + O ₂ a1	BOLSIG+		—	-0.98	
G ₁₈	E + O ₂ -> E + O ₂ b1	BOLSIG+		—	-1.63	
G ₁₉	E + O ₂ -> E + O ₂ *	BOLSIG+		—	-4.5	
G ₂₀	E + O ₂ -> E + O ₂ (electronic exc.)	BOLSIG+			-6.0	6.0
G ₂₁	E + O ₂ -> E + O ₂ (electronic exc.)	BOLSIG+			-8.4	8.4
G ₂₂	E + O ₂ -> E + O ₂ (electronic exc.)	BOLSIG+			-9.97	9.97
G ₂₃	E + O ₂ -> E + O + O	BOLSIG+			-5.58	5.58
G ₂₄	E + O ₂ -> E + O + O (electronic exc.)	BOLSIG+			-8.4	8.4
G ₂₅	E + O ₂ -> E + E + O ₂ ⁺	BOLSIG+			-12.07	—
G ₂₆	E + O -> E + O	BOLSIG+			-6.34	6.34
G ₂₇	E + O ₂ ⁺ -> O + O	BOLSIG+	6.91	—		
G ₂₈	E + O ₄ -> O ₂ + O ₂	BOLSIG+	12.07	—		
G ₂₉	E + O ₂ -> O ⁻ + O	BOLSIG+	-4.66	—		
G ₃₀	E + O ₂ a1 -> E + O ₂ b1	BOLSIG+	-0.65	—		
G ₃₁	E + O ₂ a1 -> E + O + O	BOLSIG+	-6.34	—		
G ₃₂	E + O ₂ a1 -> O ⁻ + O	BOLSIG+	-3.9	—		
G ₃₃	E + O ₂ b1 -> O ⁻ + O	BOLSIG+	-3.7	—		
G ₃₄	N ₂ ⁺ + N ₂ + M -> N ₄ ⁺ + M	5.0e-41	0	0		
G ₃₅	N ₄ ⁺ + O ₂ -> O ₂ ⁺ + N ₂ + N ₂	2.5e-16	0	0	—	3.51
G ₃₆	N ₂ ⁺ + O ₂ -> O ₂ ⁺ + N ₂	1.04e-15	-0.5	0	—	3.51
G ₃₇	O ₂ ⁺ + N ₂ + N ₂ -> O ₂ + N ₂ + N ₂	8.1e-38	-2.0	0.0	—	—
G ₃₈	O ₂ + N ₂ + N ₂ -> O ₂ ⁺ + N ₂ + N ₂	14.8	-5.3	2357.0	—	—
G ₄₉	O ₂ + N ₂ + O ₂ -> O ₄ ⁺ + N ₂	1.0e-15	0	0	—	—
G ₄₀	O ₂ ⁺ + N ₂ + M -> O ₄ ⁺ + M	2.03e-34	-3.2	0	—	—
G ₄₁	E + O ₂ + O ₂ -> O ₂ ⁻ + O ₂	6e-39	-1.0	0	—	0.43
G ₄₂	O ₂ ⁻ + O ₄ ⁺ -> O ₂ + O ₂ + O ₂	1e-13	0	0	—	11.64
G ₄₃	O ₂ ⁻ + O ₄ ⁺ + M -> O ₂ + O ₂ + O ₂ + M	3.12e-31	-2.5	0	—	11.64
G ₄₄	O ₂ ⁻ + O ₂ ⁺ + M -> O ₂ + O ₂ + M	3.12e-31	-2.5	0	—	11.64
G ₄₅	O ⁻ + O ₂ ⁺ -> O + O ₂	3.464e-12	-0.5	0	—	10.61
G ₄₆	N ₂ A + O ₂ -> N ₂ + O + O	1.7e-18	0	0	—	1.05
G ₄₇	N ₂ A + O ₂ -> N ₂ + O ₂ b1	7.5e-19	0	0	—	4.54
G ₄₈	N ₂ A + N ₂ A -> N ₂ + N ₂ B	7.7e-17	0	0	—	4.99
G ₄₉	N ₂ A + N ₂ A -> N ₂ + N ₂ C	1.6e-16	0	0	—	1.31
G ₅₀	N ₂ A + N ₂ -> N ₂ + N ₂ B	1.0e-16	0	1500.0	—	0.32
G ₅₁	N ₂ A + O -> N ₂ + O	3.0e-17	0	0	—	6.17
G ₅₂	N ₂ B + O ₂ -> N ₂ + O + O	3.0e-16	0	0	—	2.23
G ₅₃	N ₂ B + N ₂ -> N ₂ A + N ₂	1.0e-17	0	0	—	1.18
G ₅₄	N ₂ a1 + O ₂ -> N ₂ + O + O	2.8e-17	0	0	—	3.28
G ₅₅	N ₂ a1 + N ₂ -> N ₂ + N ₂	2.0e-19	0	0	—	8.4
G ₅₆	N ₂ C + O ₂ -> N ₂ + O + O	3.0e-16	0	0	—	5.91
G ₅₇	N ₂ C + N ₂ -> N ₂ a1 + N ₂	1.0e-17	0	0	—	2.63
G ₅₈	N ₂ C -> N ₂ B	3e7	0	0	—	—
G ₅₉	O ₂ * + O ₂ -> O ₂ a1 + O ₂	1.86e-19	0	0	—	3.52

Table 3. (Continued.)

Rxn	Reaction	A (molecules-m)	B (non-dim)	C (Kelvin)	$\Delta E_{\text{electron}}$ (eV)	$\Delta E_{\text{background}}$ (eV)
G ₆₀	$\text{O}_2^* + \text{O}_2 \rightarrow \text{O}_2\text{b1} + \text{O}_2$	8.1e-20	0	0	—	2.87
G ₆₁	$\text{O}_2^* + \text{O}_2 \rightarrow \text{O}_2 + \text{O}_2$	2.3e-20	0	0	—	4.5
G ₆₂	$\text{O}_2^* + \text{O} \rightarrow \text{O}_2 + \text{O}$	5.0e-18	0	0	—	4.5
G ₆₃	$\text{O}_2^* + \text{O} \rightarrow \text{O}_2\text{a1} + \text{O}$	2.7e-18	0	0	—	3.52
G ₆₄	$\text{O}_2^* + \text{O} \rightarrow \text{O}_2\text{b1} + \text{O}$	1.35e-18	0	0	—	2.87

electron carries with it when it is ejected and is specified as an input

$$\vec{\Gamma}_e \cdot \hat{n} = 2k_b T_e \frac{1}{4} n_k \sqrt{\frac{8k_b T_k}{\pi m_k}} - \sum_i e \cdot E_{e,k} \gamma_i \vec{\Gamma}_i \cdot \hat{n}. \quad (9)$$

At the sides/far field regions symmetric boundary conditions are used. Symmetric boundary condition specify that the value of the conserved variable (electrostatic potential, species densities and energies) are mirrored at the boundary. At axis boundaries, the net flux of species densities and energies are set to zero based on the principle that an axis face has zero area.

The gas-species transport formulation for plasma is implemented in the GASACT species properties and chemistry library that is part of the VizGlow software package [19]. The species diffusion coefficient, D_k , the species mobility (for charged species), μ_k , and the species thermal conductivity, k_k , can be defined in terms of the collision frequency, $\bar{\nu}_{kb}$, as follows:

$$D_k = \frac{k_B T_{k,eff}}{m_k \bar{\nu}_{kb}} \quad \mu_k = \frac{Z_k e}{m_k \bar{\nu}_{kb}} \quad k_k = \frac{5}{2} k_B D_k n_k. \quad (10)$$

The transport properties assume a Maxwellian or a near-Maxwellian distribution function for the species. However, especially in the case of electrons, the velocity distribution function can be significantly different from a Maxwellian. VizGlow provides flexibility to nominally correct for these errors. A pre-factor multiplier can be specified for all of the above species transport properties, and in particular for the species collision frequency, as follows:

$$\bar{\nu}_{kb} = \xi_{\nu_k} \bar{\nu}_{kb,orig}. \quad (11)$$

A plasma chemical kinetic mechanism for air (N_2 and O_2) is used in this study. The mechanism consists of a total of 18 species: E, O_2 , O_2^* , $\text{O}_2\text{a1}$, $\text{O}_2\text{b1}$, O_2+ , O_2- , O, O_4+ , $\text{O}_2 + \text{N}_2$, N_2 , $\text{N}_2\text{a1}$, N_2A , N_2B , N_2C , N_2+ , N_4+ . Here, E is electrons, O_2^* is the excited Herzberg state, $\text{O}_2\text{a1}$ is the singlet delta, and $\text{O}_2\text{b1}$ is a singlet sigma excited states of molecular oxygen, $\text{N}_2\text{a1}$, N_2A , N_2B , and N_2C are electronically states of molecular nitrogen, species symbols with '+' indicate positive ions, and '-' indicate negative ions. We also note cluster ions O_4+ , $\text{O}_2 + \text{N}_2$, and N_4+ that are stable forms. Table 2 in [20] provide additional information on these species. The chemistry mechanism comprises reaction rate pathways from the literature [21–23] and shown in table 3.

In table 3, reactions are either Arrhenius reaction rates or they are generated and tabulated from cross-section data. If a reaction is not labeled BOLSIG+ then it is an Arrhenius

reaction rate. The letter A, B and C are terms in the Arrhenius rate coefficient formula given by

$$k = AT^B e^{-\frac{T}{C}}. \quad (12)$$

All reactions labeled BOLSIG+ are a function of the electron temperature, T_e , while the reaction rates involving neutrals (given as Arrhenius reaction rates), are a function of a single heavy species temperature, T_g . Electron impact reactions of O_2 and N_2 were generated using the offline Boltzmann solver BOLSIG+ [24] and the cross-sectional data for N_2 and O_2 [22]. While the electron properties, including mobility, were calculated using BOLSIG+, the electron collision frequency multiplier was used in this study as a tuning parameters to account for the general uncertainty that exists in determining the collision cross-section of the electron impact reactions.

Electron impact reactions with oxygen and nitrogen molecules can lead to several different excited energy states of both short and long life times. In this mechanism, rotational and vibrational excited states are not explicitly tracked, but the loss of electron energy in generating these excited modes is accounted for in the reaction mechanism. Several electronically excited species of nitrogen and oxygen are however explicitly represented as individual species with the corresponding production/destruction pathways in the mechanism.

Streamer discharges (in particular positively charged or cathode-directed) require an initial seed electron charge distribution to propagate. An important physical process that provides electron seed charge for the streamer to propagate is photoionizing radiation emitted by the active ionizing zone of the streamer. In this study, we utilize an air photoionization model based on the three-term exponential Helmholtz model described in detail in Bourdon *et al* [25] and used in prior numerical studies on streamer discharges for atmospheric pressure plasma jets [26]. The radiation source term for ionization of oxygen due to photoemission from electron impact of nitrogen can be modeled using a volume integral model described by Zheleznyak *et al* [27]. While the integral model is simple, it must be evaluated for every emission cell/absorption cell pair and can be computational very expensive. The Helmholtz model approximates the full integral which solves three Helmholtz equations for three contributions. The sum of the contributions provides the volumetric photoionizing source term. The three-term Helmholtz model is significantly more efficient from computation standpoint with minimal loss of accuracy [25]. In air, the model assumes that the emission of ionizing photons is proportional to electron impact ionization of nitrogen molecules. The emitted radiation has wavelengths

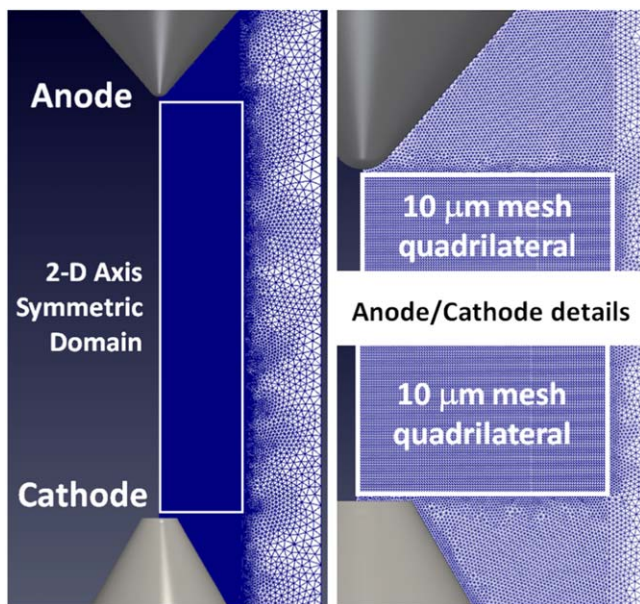


Figure 3. Computational domain and mesh details.

in the range of 98–102.5 nm (~ 12.1 – 12.65 eV) which are sufficient to ionize oxygen molecules.

Simulation setup

Computational domain and mesh characteristics are illustrated in figure 3. An axisymmetric two-dimensional domain was chosen for this study. Main features are the two concentric electrodes, a round-tip anode (top electrode) and a flat top cathode (bottom electrode), the centerline, and outer boundaries away from the electrode gap. Electrode profiles match the nominal dimensions that were measured in experiments. The anode tip radius is $125\ \mu\text{m}$, and the cathode tip has a flat top surface with a diameter of $0.44\ \text{mm}$. The inter-electrode tip-to-tip gap size is $5.2\ \text{mm}$ and is fixed in all the simulations performed here. The computational mesh is made of mixed triangle and quadrilateral cells. Small triangle cells are used at the electrode surfaces to properly account for the electrode geometry. The triangle cells then transit to quadrilateral cells with a fixed cell length ($10\ \mu\text{m}$, i.e. the minimum cell size) in the central gap region identified by the white rectangle in figure 3. This is the region where the streamers are formed and propagate. In regions away from the gap centerline, a progressively coarser triangle mesh is generated to keep relatively low total cell counts ($\approx 80\ 000$), thereby reducing simulation time. The smallest cell size is $10\ \mu\text{m}$, which delivers a good compromise between accuracy and simulation time. The analysis of the impact of mesh resolution on this type of simulations was performed in a previous study [18].

The centerline features an axis boundary condition that ensures three-dimensional symmetry, with open surface symmetry boundaries at the outer edge of the domain. The electrode surfaces are treated as equipotential surfaces for the electrostatic potential solution and as solid surfaces with wall boundary processes for the species density and temperature equations. Raw profiles from the experiments (shown in

figure 2) are applied to the anode as voltage boundary condition.

The initial gas temperature is $343\ \text{K}$ (corresponding to $70\ ^\circ\text{C}$), with the gas composed of 20.95% O_2 and 79.05% N_2 in volume fractions. The initial electron number density is set at $10^9\ \text{m}^{-3}$, which is also the default ground level for all the involved species other than O_2 and N_2 . The initial electron number density has been found to significantly impact the time required for the streamer to emerge within the gap [17], also referred as to induction time. However, preliminary calculations not shown in this paper have confirmed this finding, but also shown that the streamer induction time does not affect the LTP-to-arc pressure threshold.

Finally, in order to resolve the dynamics of the nanosecond discharge, a fixed time step of $2 \times 10^{-13}\ \text{s}$ was used. The total physical time simulated was about $150\ \text{ns}$ depending on the specific operating conditions. For each of these conditions, simulations were carried out for as long as the applied voltage was high enough to impact the streamers characteristics.

As a summary, compared to previously published numerical and experimental work [18], the gap distance increased slightly ($5.2\ \text{mm}$ versus $5.0\ \text{mm}$), the cathode geometry changed (flat top versus round tip), and the concentration was pure desiccated air (versus a mixture of oxygen and nitrogen with the addition of small components that were not quantified). Also, several maximum voltage values were investigated (i.e. 10.3 , 14.4 , 19.2 and $22.5\ \text{kV}$) and the LTP-to-arc transition for all of those voltage settings was calculated and validated against experiments. Furthermore, for the first time to the best of our knowledge, in this paper the experimental measurement of temperature and atomic oxygen in the proximity of the anode was targeted by simulations in order to deliver a quantitatively validated numerical methodology.

Results and discussion

Results will be illustrated according to the following order: first, the calibration of the model to match experimental data will be discussed, based on previous findings; next, the comparison with experimental data will be shown in a quantitative fashion, for both the LTP-to-arc transition and the plasma characteristics; finally, insight into the streamer propagation mechanisms as well as the post-discharge streamer properties will be provided; finally, additional considerations introducing future research studies will be provided.

Model calibration

Previous numerical studies performed at Argonne [18] showed that the transient plasma model is capable of matching the experimental observations in terms of streamers' behavior and appearance: higher pressure in the gap delivered slower, thinner streamers with higher tendency to branch. Also, the distribution of atomic oxygen and temperature seemed to qualitatively match corresponding images of electronically excited atomic oxygen after the discharge and schlieren images of density gradients from Sandia [14]. The main disagreement that was

Table 4. Comparison between experiments and modeling in terms of post-discharge regime.

V_{peak} (kV)	Experiments		Modeling (before tuning) Transition from Spark (arc) to glow (LTP)	Modeling (after tuning) Transition from Spark (arc) to glow (LTP)
	Arc probability 100% (Spark)	Arc probability 0% (Glow)		
10.3	1.07	1.14		
14.4	1.33	1.45	Below 1.0 bar	Between 1.35 and 1.4 bar
19.2	1.69	1.86	Between 1.0 and 1.2 bar	Between 1.8 and 1.9 bar
22.5	2.87	3.27		

observed concerned the transition pressure threshold between the spark (arc) and glow (LTP) regimes. Simulations performed in [18] predicted such transition at a lower pressure with respect to experiments, i.e. 1.6 bar versus 2.2–2.8 bar.

However, some potential sources for uncertainty were identified in both the experiments (exact gas composition, electrode nominal geometry, and voltage measurements) and the simulations (initial electron seeding, electrode geometry irregularities, chemical kinetics). Preliminary numerical investigations (not shown) led to the conclusion that initial electron seeding and irregularities in the electrode geometry might affect the streamer induction time (i.e. the time from the beginning of the discharge that the streamers take to start propagating from the electrodes), but ultimately have no effect on the final prediction of the discharge regime, be it either spark or glow. Therefore, while experiments focused on accurately measuring the nominal geometry, simulations focused on tuning the chemistry to match the experiments.

Results on the model calibration are shown in table 4. It is worth noting that: (1) only the intermediate voltage conditions (14.4 and 19.2 kV) were evaluated for model calibration; (2) experiments are repeated a number of times and a probability number is provided as an output, while simulations will always fall in either one of the two regimes. The non-tuned model showed a discrepancy with respect to the experiment of about 0.65 bar (for the 19.2 kV case), which is in line with previous results [18]. Tuning the electron collision frequency from the default multiplicative factor of $\xi_{\nu_E} = 1.0$ to $\xi_{\nu_E} = 0.3$ increased the LTP-to-arc transition pressure to better match the experiments.

Again, we note that this multiplicative factor accounts for model uncertainties associated with the collision cross-section used in the description of the transport properties. More details about the tuning procedure is provided in the last section of the results.

Validation against experiments

Once the model was calibrated, validation against experiments was performed. The first step was to extend the simulations to all the operating conditions evaluated in the paper. Figure 4 shows the comparison between experiments and modeling in terms of post-discharge regime for the entire experimental dataset. It is worth mentioning that simulations would not be able to capture the intermediate red region where a probability of arc between 0% and 100% was observed experimentally.

Overall, simulations do a good job reproducing the experiment results. The exception was for the lowest and highest voltage tested, which still show discrepancy (especially at the highest voltage value) between the observed and modeled breakdown limits. It is possible that the model is missing additional physics that becomes dominant at such higher voltage conditions (this is discussed further in the last section of the results). However, the linear trend captured by simulations over a relatively wide range of voltage values is justified by theoretical considerations. The post-discharge regime depends on the reduced electric field, E/N , and while the electric field E depends on the voltage, the number density is a linear function of pressure (temperature is constant in the cases analyzed in this paper). Therefore, in theory the linear trend makes adequate sense, and something else could contribute to deviate the experiments from the linear behavior.

Table 5 shows the comparison between experimental measurements and numerical calculations of the ground state of atomic oxygen and bulk gas temperature. Both measurements and calculations are performed at the same location in the proximity of the anode (shown in figure 1), and at the same pressure value. The agreement between experimental and numerical data in table 5 is good. To the authors' best knowledge, this is one-of-a-kind quantitative comparison performed in the LTP modeling literature. It can be concluded that a well-tuned model is capable of delivering accurate predictions of the relevant properties of transient plasmas.

General description of the streamer discharge

This section aims at providing more insight into the streamer propagation process and post-discharge plasma characteristics. To this purpose, figure 5 shows the evolution of the electron number density and reduced electric field E/N for both the arcing and non-arcing conditions calculated with a nominal voltage of 14.4 kV. It can be seen that at the threshold for glow-to-arc (spark) transitions even a small difference in the initial pressure value (1.35 versus 1.40 bar) can exhibit very different post-discharge plasma regimes. Indeed, the onset and propagation of the streamers is very similar and occurs only a bit faster (meaning that the process starts 1 ns earlier) for the lower pressure case. The entire process, including streamer propagation and connection, is consistently delayed by 1 ns at higher pressure. The only other difference is that the induction of the negative streamer is not clearly visible for the higher pressure case (1.40 bar).

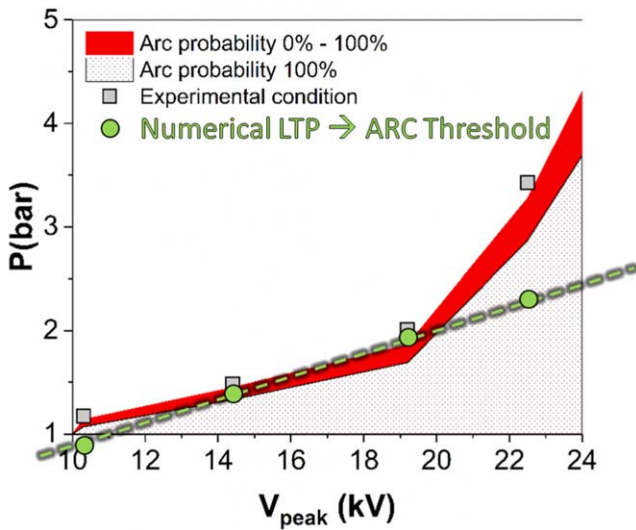


Figure 4. Comparison between experiments and simulations in term of LTP-to-arc transition.

Table 5. Comparison between experiments and simulations in terms of atomic oxygen (ground state) and temperature in the near-anode region.

Test condition	Simulation		Experiment	
	O (cm ⁻³)	T (K)	O (cm ⁻³)	T (K)
14.4 kV, 1.5 bar	0.9×10^{18}	770	1.3×10^{18}	779
19.2 kV, 2.0 bar	1.8×10^{18}	938	2.1×10^{18}	1094

However, at 87 ns and 88 ns respectively, it can be seen that both the positive and negative streamers have formed, have propagated in the gap, and have connected with each other. While visually the difference between the two pressure cases is minor, the post-discharge results are quite different.

Figure 5 shows that the solution for the lower pressure case diverged approximately 93 ns after the simulation start and is taken to be due to the onset of arcing (sparking) for which the non-equilibrium plasma formulation becomes mathematically too stiff to be properly resolved. Figure 6 shows the transient evolution of the discharge currents for the two cases. The lower pressure case is characterized by a steep increase in the electrical current at the time the positive and negative streamers connect to form a highly conducting channel in the entire gap. This increase in current corresponds to an exponential increase in the electron density, i.e. transition to arcing. As can be seen in the slightly higher pressure (1.40 bar) the increase of current is followed by a current drop while the plasma remains in an LTP glow state.

Figure 7 shows the thermal (bulk gas temperature) and chemical (ground state atomic oxygen) plasma characteristics at the end of the discharge, after the voltage has dropped to very low values. The above-arc pressure conditions (i.e. 1.40 and 1.90 bar) are shown for discharges with the peak voltages of 14.4 kV and 19.2 kV respectively. Higher pressure values show tendency to branch, which again matches experimental

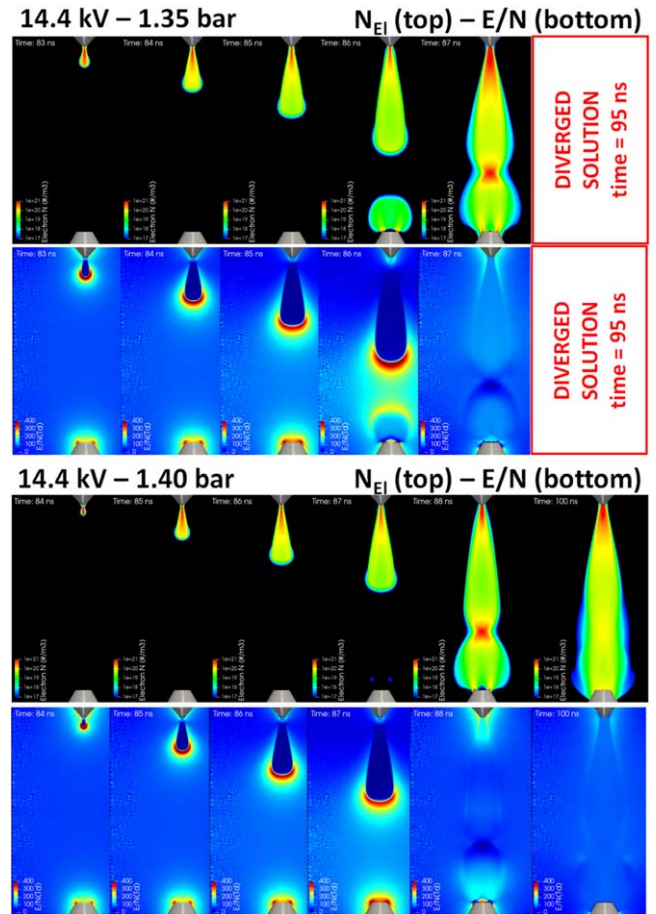


Figure 5. Streamer propagation mechanism in the spark (1.35 bar) and glow (1.40 bar) regimes for an applied peak voltage of 14.4 kV.

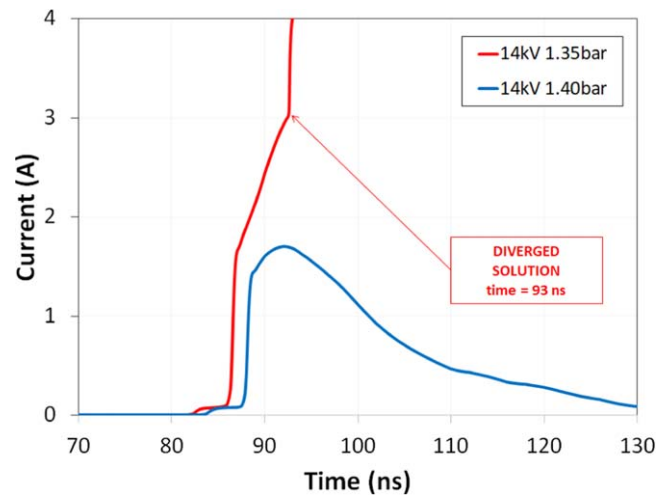


Figure 6. Electrical current profile for spark (1.35 bar) and glow (1.40 bar) regimes for an applied peak voltage of 14.4 kV.

observations. In general, it must be highlighted here that the gas temperature is greater than the initial values, and actually reaches out fairly high (>1000 K) values in the proximity of the anode. This location corresponds to the region where also the production of atomic oxygen is the highest.

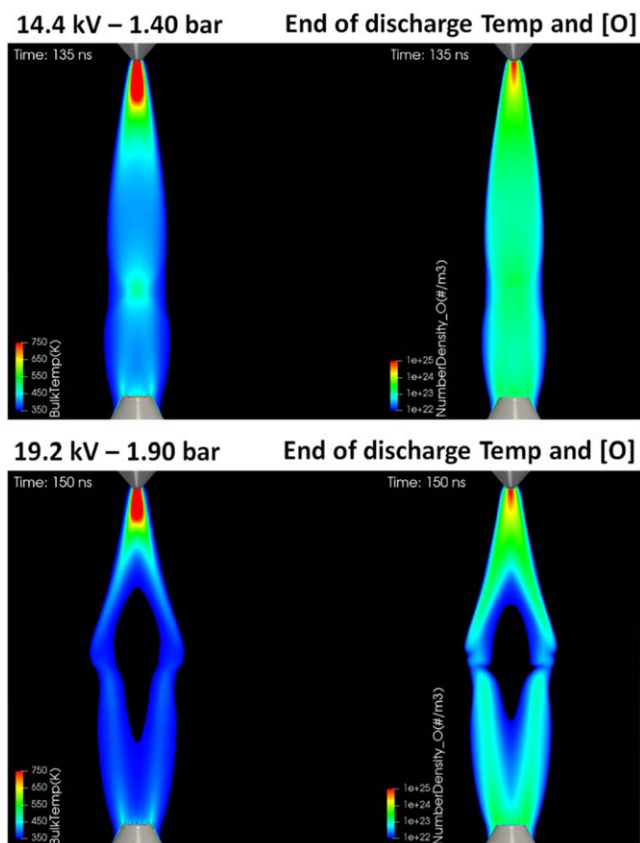


Figure 7. Thermal (Temperature) and chemical (atomic oxygen) plasma properties at the end of the discharge (main pulse) for 14.4 and 19.2 kV at near-arc conditions.

It is worth noting that the geometry of the electrodes dictates where the highest temperature values and radical production are located. In the case of the geometry evaluated in this paper, the anode has a sharper tip compared to the cathode flat top surface, therefore the streamer will generate and propagate first from the anode. Also, for the same reason, the local electric field enhancement will be larger in the proximity of the anode, resulting in higher temperature and production of active species. Overall, distribution of temperature and active species that trigger the ignition process at a later stage is what is needed to investigate LTP ignition processes. Once again it is shown in figure 7 that the higher the pressure, the less uniform the plasma characteristics are (also due to increased branching), thus requiring multi-dimensional numerical tools for proper analysis.

Further considerations and future steps

The goals of this paper as defined in the introduction (i.e. improving the agreement between experiments and modeling, and provide quantitative validation of plasma properties) were successfully met, yet margins for potential improvement of the numerical methodology proposed in this study can be identified.

We have found that within the context of the non-equilibrium plasma fluid model the results are sensitive to the

electron collision frequency that enter the description of the electron transport properties. We have used this as an effective tuning/calibration parameter for the model, justifying this based on the general uncertainty that exists in determining the collision cross-section of the electrons in a complex chemical environment under very high driving electric field conditions. Other simulation parameters (in particular the initial electron seeding and geometry irregularities) and their effect on the LTP-to-arc transition pressure threshold need to be explored further, although preliminary studies delivered a negligible impact on the post-discharge regime. Uncertainties associated with the plasma chemistry and in particular the cross sections of electron impact reactions (that are of most relevance to fast transient phenomena in streamers) are a subject of ongoing studies by various investigators [28, 29]. We note that, despite the many different sources of model uncertainties, we have found that a single parameter, i.e. electron collision frequency, provided an opportunity for fast calibration of the model to achieve good quantitative agreement with experiments. This does not mean that the electron collision frequency is 70% wrong. The discrepancy between the multiplier values 0.3 and 1.0 simply accounts with potentially other uncertainties that we still have not explored. As an example, in the real case, flow and slow heating of the channel (the phase after the streamer forms where the reduced electric field slowly builds up as the channel heats) are crucial physics that should be taken into account. Coupling the flow physics and capturing gas channel heating and relaxation could be important for more accurately predicting the transition and is another source of uncertainty.

As far as the comparison between experiments and simulations shown in figure 4 is concerned, it is observed that the model calibration does not remove the discrepancy entirely, especially when a large range of conditions are simulated. Furthermore, the role of voltage oscillations (ringing) and their impact on plasma discharge and post-discharge ignition remains to be studied. Indeed, it was noticed that the voltage oscillations after the main pulse were wider for the 22.5 kV nominal case with respect to the other conditions.

In general, the information provided by non-equilibrium plasma models are very valuable to evaluate the LTP ignition mechanism. Specifically, the post-discharge plasma properties and also the impact of the post-discharge conditions on subsequent pulses, when the nanosecond pulsed discharge is operated in a multi-pulse fashion can be studied readily. Ultimately, our research will focus on the LTP ignition mechanism and a more comprehensive chemical scheme that can model the transition from LTP plasma into an actual flame, to be used for modeling PAI applications.

Conclusions

A numerical methodology was used in this study to investigate the effect of nanosecond pulsed discharge on the plasma characteristics, including the post-discharge regime and the

thermal and chemical properties of transient plasma in a glow (LTP) regime. Main conclusions are listed as follows:

- Previous numerical results were confirmed, in that an offset of about 0.6–0.7 bar between modeling and experiments was found when calculating the pressure value for the regime transition from spark into glow. Simulations under-predicted the transition pressure value, consistently with the previous study.
- Some experimental uncertainties, including gas composition and electrode geometries, were removed as well as some numerical uncertainties, mainly concerning the initial (seeding) and boundary (geometry tolerance) conditions.
- Rather than tuning all other possible sources of uncertainty, we chose to look at sensitivity to electron collision frequency as a single tuning parameter. A calibrated model was capable of reducing the gap between modeling and experiments and improve the numerical prediction of the plasma regime on quantitative basis.
- While some discrepancies remained right at the boundaries of the experimental dataset (low and high-voltage conditions), the quantitative agreement between simulations and experiments in terms of certain thermal (temperature) and chemical (atomic oxygen) plasma properties was good.
- The evaluation of the discharge in both glow and spark regime showed that the numerical tool used in this study is capable of providing a comprehensive characterization of the two regimes' boundaries, although it cannot fully handle simulations in the spark regime.
- Future studies will be looking at further improving the current numerical predictions and transitioning into investigating the LTP ignition mechanism.

Acknowledgments

The submitted manuscript has been created by UChicago Argonne, LLC, Operator of Argonne National Laboratory ('Argonne'). Argonne, a US Department of Energy Office of Science laboratory, is operated under Contract No. DE-AC02-06CH11357. The US Government retains for itself, and others acting on its behalf, a paid-up nonexclusive, irrevocable worldwide license in said article to reproduce, prepare derivative works, distribute copies to the public, and perform publicly and display publicly, by or on behalf of the Government.

This research is funded by DOE's Vehicle Technologies Program, Office of Energy Efficiency and Renewable Energy. The authors would like to express their gratitude to Gurpreet Singh, Mike Weismiller, and Leo Breton (retired), program managers at DOE, for their support. Numerical simulations were run on the Bebop Cluster at the LCRC facility, Argonne National Laboratory.

ORCID iDs

Riccardo Scarcelli  <https://orcid.org/0000-0003-3989-3611>
 Sayan Biswas  <https://orcid.org/0000-0001-8427-1569>

References

- [1] Briggs T, Alger T and Mangold B 2014 Advanced ignition systems evaluations for high-dilution SI engines *SAE Int. J. Engines* **7** 1802–7
- [2] Sevik J, Wallner T, Pamminger M, Scarcelli R *et al* 2016 Extending lean and exhaust gas recirculation-dilute operating limits of a modern gasoline direct-injection engine using a low-energy transient plasma ignition system *J. Eng. Gas Turbines Power* **138** 112807
- [3] Sjöberg M, Zeng W, Singleton D, Sanders J M *et al* 2014 Combined effects of multi-pulse transient plasma ignition and intake heating on lean limits of well-mixed E85 DISI engine operation *SAE Int. J. Engines* **7** 1781–801
- [4] Starikovskaia S M 2006 Plasma assisted ignition and combustion *J. Phys. Appl. Phys.* **39** R265
- [5] Starikovskaia S M 2014 Plasma-assisted ignition and combustion: nanosecond discharges and development of kinetic mechanisms *J. Phys. Appl. Phys.* **47** 353001
- [6] Wolk B, DeFilippo A, Chen J-Y, Dibble R *et al* 2013 Enhancement of flame development by microwave-assisted spark ignition in constant volume combustion chamber *Combust. Flame* **160** 1225–34
- [7] Nishiyama A and Ikeda Y 2012 Improvement of lean limit and fuel consumption using microwave plasma ignition technology *SAE Technical Paper* 2012-01-1139 SAE (<https://doi.org/10.4271/2012-01-1139>)
- [8] Chintala N, Bao A, Lou G and Adamovich I V 2006 Measurements of combustion efficiency in nonequilibrium RF plasma-ignited flows *Combust. Flame* **144** 744–56
- [9] Hampe C, Kubach H, Spicher U and Rixecker G 2013 Investigations of ignition processes using high frequency ignition *SAE Technical Paper* 2013-01-1633 SAE (<https://doi.org/10.4271/2013-01-1633>)
- [10] Singleton D *et al* 2011 The role of non-thermal transient plasma for enhanced flame ignition in C₂H₄–air' *J. Phys. D: Appl. Phys.* **44** 022001
- [11] Pendleton S J *et al* 2013 The production and evolution of atomic oxygen in the afterglow of streamer discharge in atmospheric pressure fuel/air mixtures *J. Phys. D: Appl. Phys.* **46** 305202
- [12] Pai D Z, Lacoste D A and Laux C O 2010 Transitions between corona, glow, and spark regimes of nanosecond repetitively pulsed discharges in air at atmospheric pressure *J. Appl. Phys.* **107** 093303
- [13] Wolk B and Ekoto I 2017 Calorimetry and atomic oxygen laser-induced fluorescence of pulsed nanosecond discharges at above-atmospheric pressures *Ignition Systems for Gasoline Engines* (Cham: Springer International Publishing) pp 169–89
- [14] Wolk B M and Ekoto I 2017 Calorimetry and imaging of plasma produced by a pulsed nanosecond discharge igniter in EGR gases at engine-relevant densities *SAE Int. J. Engines* **10** 970–83
- [15] Ju Y and Sun W 2015 Plasma assisted combustion: dynamics and chemistry *Prog. Energy Combust. Sci.* **48** 21–83
- [16] Tholin F Bourdon A 2011 Influence of temperature on the glow regime of a discharge in air at atmospheric pressure between two point electrodes *J. Phys. Appl. Phys.* **44** 385203

- [17] Tholin F and Bourdon A 2013 Simulation of the stable ‘quasi-periodic’ glow regime of a nanosecond repetitively pulsed discharge in air at atmospheric pressure *Plasma Sources Sci. Technol.* **22** 045014
- [18] Scarcelli R, Zhang A, Wallner T, Breden D *et al* 2018 Multi-dimensional modeling of non-equilibrium plasma for automotive applications *SAE Technical Paper 2018-01-0198* (<https://doi.org/10.4271/2018-01-0198>)
- [19] VizGlow Theory Manual 2016 Plasma modeling software for multi-dimensional simulations of non-equilibrium glow discharge systems (Austin, TX: Esgee Technologies Inc) <http://esgeetech.com/>
- [20] Breden D, Raja L L, Idicheria C A, Najt P M *et al* 2013 A numerical study of high-pressure non-equilibrium streamers for combustion ignition application *J. Appl. Phys.* **114** 083302
- [21] Pancheshnyi S, Nudnova M and Starikovskii A 2005 Development of a cathode-directed streamer discharge in air at different pressures: experiment and comparison with direct numerical simulation *Phys. Rev. E* **71** 016407
- [22] Kossyi I A, Kostinsky A Y, Matveyev A A and Silakov V P 1992 Kinetic scheme of the non-equilibrium discharge in nitrogen-oxygen mixtures *Plasma Sources Sci. Technol.* **1** 207
- [23] Aleksandrov N, Kindysheva S, Kukaev E, Starikovskaya S and Starikovskii A 2009 Simulation of the ignition of a methane-air mixture by a high voltage nanosecond discharge’ *Plasma Phys. Rep.* **25** 867–82
- [24] Hagelaar G J M and Pitchford L C 2005 Solving the Boltzmann equation to obtain electron transport coefficients and rate coefficients for fluid models *Plasma Sources Sci. Technol.* **14** 722–33
- [25] Bourdon A, Pasko V P, Liu N Y, Celestin S, Segur P and Marode E 2007 Efficient models for photoionization produced by non-thermal gas discharges in air based on radiative transfer and the Helmholtz equations *Plasma Sources Sci. Technol.* **16** 656–78
- [26] Breden D, Miki K and Raja L L 2012 Self-consistent two-dimensional modeling of cold atmospheric-pressure plasma jets/bullets *Plasma Sources Sci. Technol.* **21** 034011
- [27] Zheleznyak M B, Mnatsakanyan A K and Szykh S V Photoionization of nitrogen and oxygen mixtures by radiation from a gas discharge *High Temp.* **20** 357–62
- [28] Kieffer L J and Dunn G H 1966 Electron impact ionization cross_section data for atoms, atomic ions, and diatomic molecules: I. Experimental data *Rev. Mod. Phys.* **38** 1–35
- [29] Pancheshnyi S, Biagi S, Bordage M C, Hagelaar G J M *et al* 2012 The LXCat project: electron scattering cross sections and swarm parameters for low temperature plasma modeling *Chem. Phys.* **398** 148–53